Tuning Bifunctional Oxygen Electrocatalysts by Changing the A-Site Rare-Earth Element in Perovskite Nickelates

Le Wang, Kelsey A. Stoerzinger,* Lei Chang, Jiali Zhao, Yangyang Li, Chi Sin Tang, Xinmao Yin, Mark E. Bowden, Zhenzhong Yang, Haizhong Guo, Lu You, Rui Guo, Jiaou Wang, Kurash Ibrahim, Jingsheng Chen, Andrivo Rusydi, Junling Wang,* Scott A. Chambers, and Yingge Du*

Perovskite-structured (ABO_3) transition metal oxides are promising bifunctional electrocatalysts for efficient oxygen evolution reaction (OER) and oxygen reduction reaction (ORR). In this paper, a set of epitaxial rare-earth nickelates ($RNiO_3$) thin films is investigated with controlled A-site isovalent substitution to correlate their structure and physical properties with ORR/OER activities, examined by using a three-electrode system in O_2-saturated 0.1 M KOH electrolyte. The ORR activity decreases monotonically with decreasing the A-site element ionic radius which lowers the conductivity of $RNiO_3$ (R = La, $La_{0.5}Nd_{0.5}$, $La_{0.2}Nd_{0.8}$, Nd, $Nd_{0.5}Sm_{0.5}$, Sm, and Gd) films, with $LaNiO_3$ being the most conductive and active. On the other hand, the OER activity initially increases upon substituting La with Nd and is maximal at $La_{0.2}Nd_{0.8}NiO_3$. Moreover, the OER activity remains comparable within error through Sm-doped $NdNiO_3$. Beyond that, the activity cannot be measured due to the potential voltage drop across the film. The improved OER activity is ascribed to the partial reduction of Ni^{3+} to Ni^{2+} as a result of oxygen vacancies, which increases the average occupancy of the e_g antibonding orbital to more than one. The work highlights the importance of tuning A-site elements as an effective strategy for balancing ORR and OER activities of bifunctional electrocatalysts.

1. Introduction

Predictive synthesis of highly active and cost-effective electrocatalysts for energy conversion and storage has become critical in leveraging intermittently available renewable energy sources.[1–3] Oxygen reduction reaction (ORR) and oxygen evolution reaction (OER) are two of the most important electrochemical reactions that limit the efficiencies of fuel cells, metal-air batteries, and electrolytic water-splitting.[4–7] Although some noble metals and their associated compounds, such as Pt, RuO_2, and IrO_2, exhibit high ORR or OER catalytic activity,[8–12] the high cost and scarcity of such precious metals prevent their large-scale use.[13,14]

Dr. L. Wang, Dr. K. A. Stoerzinger, Dr. Z. Yang, Dr. S. A. Chambers, Dr. Y. Du
Physical and Computational Sciences Directorate
Pacific Northwest National Laboratory
Richland, WA 99354, USA
E-mail: kelsey.stoerzinger@pnnl.gov; yingge.du@pnnl.gov

Dr. L. Wang, L. Chang, Dr. L. You, Prof. J. Wang
School of Materials Science and Engineering
Nanyang Technological University
Singapore 639798, Singapore
E-mail: jlwang@ntu.edu.sg

J. Zhao, Prof. J.-O. Wang, Prof. K. Ibrahim
Beijing Synchrotron Radiation Facility
Institute of High Energy Physics
Chinese Academy of Sciences
Beijing 100039, China

J. Zhao
University of Chinese Academy of Sciences
Beijing 100049, China

The ORCID identification number(s) for the author(s) of this article can be found under https://doi.org/10.1002/adfm.201803712.

DOI: 10.1002/adfm.201803712

Dr. Y. Li, Dr. R. Guo, Prof. J. Chen
Department of Material Science & Engineering
National University of Singapore
Singapore 117575, Singapore

C. S. Tang
NUS Graduate School for Integrative Sciences and Engineering
National University of Singapore
Singapore 117456, Singapore

Dr. X. Yin, Prof. A. Rusydi
Department of Physics
Faculty of Science
National University of Singapore
Singapore 117542, Singapore

Dr. M. E. Bowden
Environmental Molecular Sciences Laboratory
Pacific Northwest National Laboratory
Richland, WA 99352, USA

Prof. H. Guo
School of Physical Engineering
Zhengzhou University
Zhengzhou, Henan 450001, China

Recently, several cost-effective perovskite-structured oxides have been identified as robust, bifunctional catalysts with high ORR and OER activities.[15–19] With a general formula of ABO_3, perovskite oxides are a very important class of functional materials that exhibit a diverse range of intriguing properties and functionalities. The flexibility of the perovskite structure provides a great opportunity to tune their physical and chemical properties by varying the size and chemistry of the A- or B-site elements. The study of perovskites as epitaxial thin films enables measurement of their intrinsic catalytic activity, unconvoluted with effects from roughness, defects such as grain boundaries, or edges between facets. The ORR activity of perovskite oxides correlates strongly with the ability of B-site cation to adopt different valence states at the potential of oxygen reduction, observed as redox couples near the onset potential of ORR.[20] Catalytic trends with substitution of the B-site transition metal element in $LaBO_3$ (B = Cr, Mn, Fe, Co, and Ni) were studied by Sunarso et al.,[21] Celorrio et al.,[22] and Suntivich et al..[15] All these studies showed that Mn, Ni, and Co at the B site were more active than both Cr and Fe. In addition, ORR trends in manganates ($AMnO_3$) with A-site aliovalent substitution were also studied by Hyodo et al.[23] (A = $Pr_{1-x}Ca_x$), Celorrio et al.[24] (A = $La_{1-x}Ca_x$) and Stoerzinger et al.[25] (A = $La_{1-x}Sr_x$). The maximum of the ORR activity was found around x = 0.4 (formal valence $Mn^{3.4+}$) in all studies, commensurate with maximum conductivity and extractable charge at the potential of oxygen redox. For OER, the optimal activity among a range of ABO_3 perovskite oxides tends to be at an e_g occupancy close to unity, with high covalency of transition metal-oxygen bonds.[16] Furthermore, it has been suggested that oxygen deficiencies may promote OER activity.[17,26,27] This adds additional interest to the perovskite oxide family, where some compositions with an alkaline earth element at the A site can incorporate a wide range of oxygen stoichiometry,[28] from the brownmillerite (BM)-type structure, generally formulated with $ABO_{2.5}$,[29] to perovskite structure ABO_3.[16,18]

Among perovskite oxides, rare-earth nickelates ($RNiO_3$, here abbreviated RNO, where R represents rare-earth lanthanide elements) have attracted significant interest in recent years, due to their remarkable properties and potential utilization in electronics, catalysis, and energy storage.[18,30–36] Isovalent substitution of R ions in RNO can influence the rotation, tilt, and distortion of the NiO_6 octahedra, thus impacting their structural, physical, and chemical properties.[30] As shown in **Figure 1**a, while $LaNiO_3$ (LNO) is metallic at all temperatures, the other compounds of this family all exhibit a metal-to-insulator transition (MIT) at higher temperatures. The MIT temperature (T_{MI}) increases with decreasing rare-earth ionic radius.[30] Petrie et al. reported that conductive LNO films can drive the ORR and OER at low overpotentials, yielding a bifunctional catalyst that surpasses the specific activity of noble metals such as Pt in an alkaline environment.[18] Moreover, Sunarso et al. reported that substituting half of the nickel in LNO with cobalt, iron, manganese, or chromium improves the ORR onset potential.[21] For some perovskites such as LNO, a similar reaction mechanism involving four coupled proton–electron transfer steps has been proposed for both the OER and ORR, though the rate limiting steps differ.[15] Thus, it can be challenging to simultaneously optimized bifunctional activity, as the activation energy of the

rate limiting steps is coupled due to scaling relations.[37] In such cases, designing high-performance bifunctional electrocatalysts requires strategically balancing the OER and ORR activities. Given the promising ORR and OER activities of LNO, it is of great scientific and technological interest to examine the influence of different rare-earth elements of this RNO (R = La, Nd, Sm, and Gd) family on oxygen electrocatalysts.

In this work, we investigate a set of well-defined, epitaxial perovskite nickelates RNO (R = La, $La_{0.5}Nd_{0.5}$, $La_{0.2}Nd_{0.8}$, Nd, $Nd_{0.5}Sm_{0.5}$, Sm, and Gd) thin films grown on $SrTiO_3$ (STO) (001) substrates by pulsed laser deposition (PLD). Through extensive characterization and performance testing that involves in-plane transport, X-ray diffraction (XRD), X-ray absorption spectroscopy (XAS), ultraviolet photoelectron spectroscopy (UPS), and electrochemical measurements, we reveal the correlation between their physical properties and ORR/OER catalysis: Decreasing the A-site element ionic radius decreases the Ni-O hybridization, resulting in decreased ORR activity. On the other hand, an initial decrease in ionic radius enhances the OER activity, which is maximized at $La_{0.2}Nd_{0.8}NiO_3$ (L2N8NO). Further
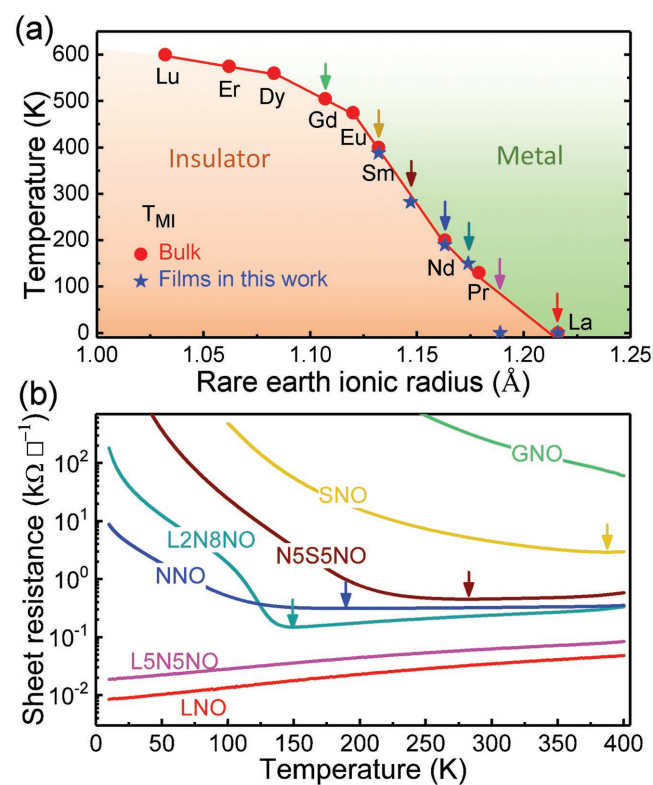

Figure 1. a) $RNiO_3$ phase diagram, with temperature along the vertical axis and rare-earth ionic radius along the horizontal axis. The red circles indicate the MIT (T_{MI}) values on warming for bulk $RNiO_3$,[30] and blue stars represent the T_{MI} values on warming for $RNiO_3$ films in the present work. Colored arrows indicate compositions studied in the present work. For GNO, this transition could not be realized in the 10–400 K temperature range of our PPMS apparatus. For mixed A-site $RNiO_3$ film, the average rare-earth ionic radius is based on the stoichiometry of the mixture. b) Sheet resistance versus temperature on warming for $RNiO_3$ films with different A-site elements on STO substrates. T_{MI} (marked by colored arrows) are defined as the temperatures of the upturn in the sheet resistance versus temperature plots.

decreasing of the average A-site radius by mixing Nd and Sm gives comparable OER activity to NdNiO$_3$ (NNO). The smaller rare-earth radius of Nd and Sm could lead to the incorporation of oxygen vacancies (V$_O$s), the corresponding Ni^{3+} → Ni^{2+} valence change resulting from V$_O$s is favorable for OER as it increases the average occupancy of the e_g antibonding orbital to more than one. Due to the potential voltage drop across the films, we cannot reliable measure OER activity at/beyond SmNiO$_3$ (SNO). Through detailed understanding of the RNO series, we find that the ORR and OER activities cannot be independently optimized, but provide new understanding in the trade-offs of designing active catalysts.

2. Results and Discussion

2.1. In-Plane Transport Properties of RNiO$_3$ Thin Films

A series of RNO thin films were deposited on STO substrates by PLD. The compositions of RNO studied in the present work are indicated by the colored arrows in Figure 1a. Details on growth conditions are given in the Experimental Section. The films were 12–15 nm thick (Table S1, Supporting Information) to ensure minimal strain relaxation. Atomic force microscope (AFM) measurements confirmed an atomically flat surface with a root-mean square roughness ≈0.2 nm over the area of 1 μm × 1 μm for these films. Figure 1b shows the sheet resistance versus temperature relationships for this series of RNO films. As the rare-earth ionic radius decreases from La to Gd, the overall sheet resistance increases continuously. This is consistent with the changes in Ni–O bond covalency, as decreasing A-site rare-earth ionic radius will bend the Ni–O–Ni angle, which reduces the orbital overlap and promotes the insulating state over the metallic phase.[30] Over the entire temperature range, LNO and La$_{0.5}$Nd$_{0.5}$NiO$_3$ (L5N5NO) show metallic behavior, while GdNiO$_3$ (GNO) shows insulating behavior. For L2N8NO, NNO, and Nd$_{0.5}$Sm$_{0.5}$NiO$_3$ (N5S5NO), metallic behavior was observed at room temperature (RT) and the MIT points (T_{MI}, noted by colored arrows in Figure 1b) are 148, 190, and 283 K, respectively. For SNO, insulating behavior is observed at RT and its T_{MI} is ≈388 K. All T_{MI} values for the RNO film series have been included in Figure 1a, marked by blue stars. Compared with bulk nickelates, T_{MI} of RNO films are slightly lower, which has been ascribed to the strain effect.[34,38]

2.2. Structural Analysis of RNiO$_3$ Thin Films

Figure 2a shows the representative XRD θ–2θ scans around (002) peak of the RNO films grown on STO substrates. The extended XRD patterns of all the compositions are

presented in Figure S1 in the Supporting Information. Well-defined Kiessig fringes can be observed, confirming the high quality of all these films. To gain additional structural information, reciprocal space maps (RSMs) near the (103) reflection of STO were measured. As shown in Figure 2b, it is clear that all the RNO films are coherently strained as their in-plane lattice parameters are the same as that of the STO substrate. Hence, the non-monotonic change observed in out-of-plane lattice parameters (OOP, Figure 2c) is not due to structural relaxation, which may provide key insights into the structure and properties of this RNO system. The pseudo-cubic lattice constants for bulk nickelates (noted by dark blue stars in Figure 2c) are smaller than that (3.905 Å) of the STO substrate. An in-plane tensile strain from the substrate would normally lead to a smaller OOP as can be estimated from its Young's modulus (noted by black open squares in Figure 2c). Indeed, the OOPs of LNO, L5N5NO, L2N8NO, and NNO films are smaller than that of the bulk, consistent with the in-plane strain effect. However, the OOPs of SNO and GNO films are larger than that of the bulk, which is due to the effect of oxygen vacancies in the films as will be discussed later.[39] From Figure 2c, the onset of the OOP's deviation from the predicted strained value suggests there should be appreciable oxygen vacancies in the L2N8NO film. Due to the presence of oxygen vacancies, a portion of
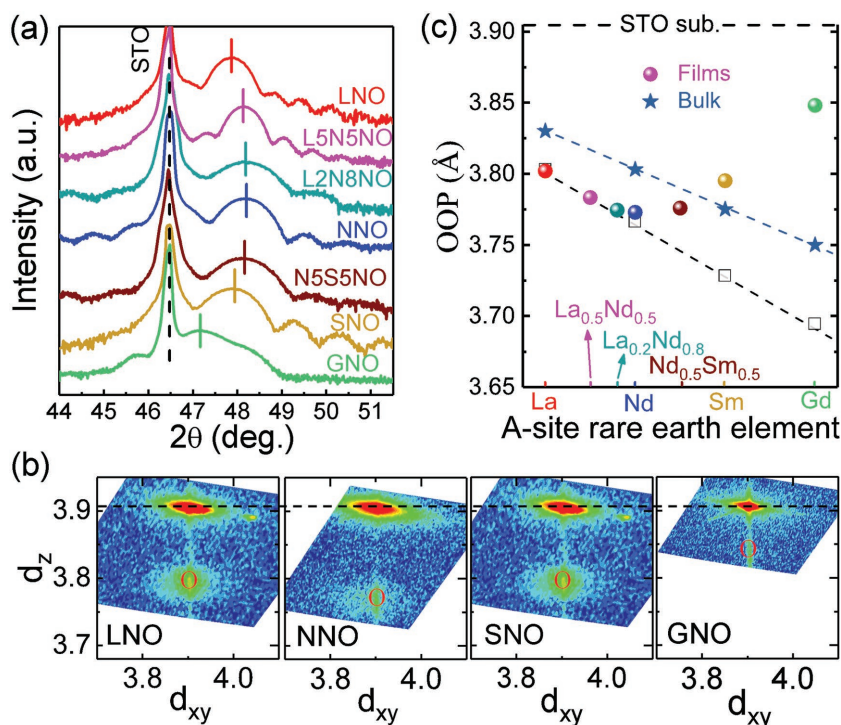

Figure 2. a) RT XRD θ–2θ scans around the (002) peaks for LNO, L5N5NO, L2N8NO, NNO, N5S5NO, SNO, and GNO films on STO substrates. The dashed line and the short color solid lines indicate the Bragg peaks from the STO substrates and the seven films, respectively. b) RSMs taken near the (103) reflection for LNO, NNO, SNO, and GNO films on STO substrates. The horizontal dashed line corresponds to the lattice parameter of the STO substrates. The open circles correspond to the lattice parameter of the RNiO$_3$ films. c) RT OOPs of RNiO$_3$ films with the A-site rare-earth element R changing from La to Gd. Dark blue stars represent the pseudocubic lattice constants for bulk LNO,[54] NNO,[55] SNO,[55] and GNO.[56] Open black squares represent the strained OOPs of RNO films estimated from the Young's modulus by taking into account the Poisson's ratio ν ≈ 0.34.[57]

**ADVANCED
SCIENCE NEWS**

www.advancedsciencenews.com

**ADVANCED
FUNCTIONAL
MATERIALS**

www.afm-journal.de

Ni ions will change from Ni^{3+} to Ni^{2+} to keep the charge neutrality, leading to a larger Ni ionic radius.[40] In addition, a larger lattice constant is also expected from "chemical expansivity" effect as a result of incorporating oxygen vacancies.[41] Due to the increase in tensile strain, more oxygen vacancies are expected to exist in the RNO films with a smaller A-site element, even if we deposited the film at the same temperature and oxygen pressure PO_2.[39,42] For Ni-containing perovskites, oxygen anion vacancies are the more likely compensation mechanism than cation vacancies.[43,44] The in-plain constraint from the substrate and out-of-plane relaxation through the formation of oxygen vacancies can thus explain the trend we observed in Figure 2.

2.3. Ni Valence and Ni–O Hybridization Changes Probed by X-Ray Absorption Spectroscopy

To corroborate the structural information obtained from Figure 2 with the electronic structure and Ni valence, we performed XAS measurements on Ni L edge (**Figure 3**a) and O K edge (Figure 3b) of the RNO films. Due to the strong overlap of the La M_4 edge with the Ni L_3 edge (Figure S2, Supporting Information), only the Ni L_2-edge spectra are used for the analysis. The spectral shape of the Ni L_2 edge strongly varies with the Ni oxidation state in Ni oxides,[39,45–48] providing insight into the Ni valence in our films. As shown in Figure 3a, the Ni L_2-edge spectra from different films are clearly different, revealing their difference in Ni valence states. For comparison, a GNO film grown at a lower PO_2 of 0.2 mTorr (GNO_0.2, bottom panel in Figure 3a) to intentionally introduce more Ni^{2+} shows an increase in the low-energy feature (labeled "α"). It is clear that when the A-site element is changed from La to Gd, the feature "α" corresponding to Ni^{2+} increases monotonically. The relatively intensity of the

two features ("α" and "β") was compared and summarized. As shown in Figure 3c, the relative intensity of the peak "α", $I_\alpha/(I_\alpha+I_\beta)$, can be used to calculate the percentage of Ni^{2+}. There is no Ni^{2+} in LNO, while the percentage of Ni^{2+} in NNO, SNO, and GNO is 6.5%, 8.9%, and 20%, respectively, suggesting that the Ni valence moves gradually towards a lower oxidation state with decreasing the ionic radius of the rare-earth element. The Ni L_2-edge spectroscopic results are in good agreement with our XRD data and support that more oxygen vacancies exist in the RNO films with smaller A-site ions. The O K-edge XAS probes the transition from the O 1s core level to unoccupied states with partial O 2p character hybridized with Ni 3d states. The intensity of the pre-peak near 528 eV originates from the $3d^8L \rightarrow c3d^8$ transition, where L and c denote a ligand and an O 1s core hole. As shown in Figure 3b, the O K-edge pre-peak intensity decreases with the decrease in rare-earth ionic radius, indicating a decrease in ligand hole density that in turn results from a decrease in Ni 3d–O 2p hybridization.[39,45] As has been shown in previous studies, the hybridization strength between metal 3d and O 2p can strongly affects the ORR activities in perovskite oxides,[15] thus its impact on the electrochemical properties of this RNO series needs to be addressed.

2.4. OER and ORR Activities

We next investigate the impact of A-site tuning on the OER and ORR activities. RNO/STO films were electrically contacted on the front and charge transport probed with the fast redox couple $[Fe(CN)_6]^{3-/4-}$ (Figure S3, Supporting Information).[25,49] Films containing some portion of La and/or Nd at the A site had sufficient conductivity to reliably measure electrocatalytic activity. For $RNiO_3$ films (SNO and GNO) with T_{MI} greater than RT, where oxygen electrocatalytic activity is measured,
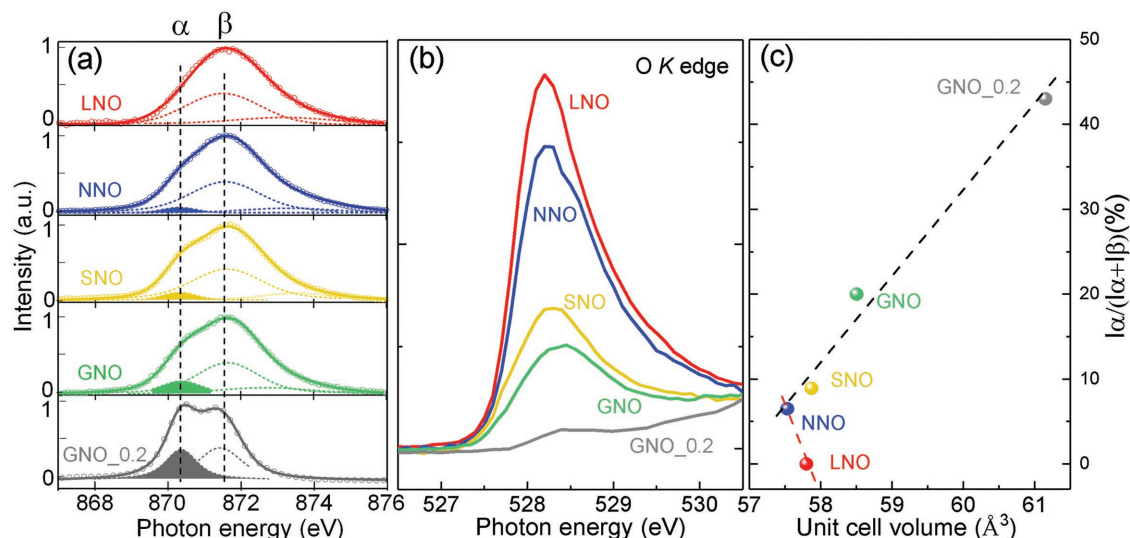

Figure 3. a) Ni L_2-edge spectra for LNO, NNO, SNO, GNO, and a reference sample GNO_0.2 (GNO film grown at 0.2 mTorr) measured at RT. The open symbols denote the experimental data. All spectra were normalized and fitted with Gaussian functions (shown as thin dashed lines). Thick solid lines are the sums of these Gaussian fits. b) O K-edge spectra for these five samples. c) The relative intensity of the peak "α", $I_\alpha/(I_\alpha + I_\beta)$, is plotted as a function of the unit cell volume.

the voltage loss in the plane of the film prohibits measurement of the intrinsic catalytic activity. So we only discuss the ORR and OER activities for $RNiO_3$ films with T_{MI} below RT. ORR and OER activities were measured in O_2-saturated 0.1 M KOH, with negligible background current measured in N_2-saturated electrolyte (Figure S4, Supporting Information). The onset potential of ORR is highest for LNO both by cyclic voltammetry (CV, **Figure 4**a) and chronoamperometry (CA, Figure 4b), with activity decreasing as Nd is substituted for La. In contrast, the incorporation of Nd improves the OER activity compared to LNO. The activity is maximum for L2N8NO by CV (Figure 4c), but comparably active with NNO by CA (Figure 4d), possibly due to some Ni oxidation current arising from the filling of surface oxygen vacancies. Further decreasing of the average A-site radius by mixing Nd and Sm gives comparable OER activity to NNO (Figure 4d), while smaller ORR activity (Figure 4b). We note that the OER Tafel slope (Figure 4d) varies amongst $RNiO_3$ films, being larger for L5N5NO ($\approx$115 mV decade^{-1}) compared to, e.g., NNO ($\approx$75 mV decade^{-1}). This may be related to the larger work function (WF) for NNO and decreased charge transfer energy, improving electron transfer.[50] However, a wide range of Tafel slopes have been observed for the OER, even at a given, e.g., charge transfer energy, so this slope is not a sole descriptor of activity or mechanism.[50]

The changes in electronic structure accessed by changing the A site in $RNiO_3$ can provide insight into oxygen electrocatalysis. The largest radius of La in $RNiO_3$ results in a highly covalent, largest Ni–O–Ni bond angle, exhibiting

metallic behavior at all temperatures. This metallic behavior is preserved in electrochemical conditions, probed with the $[Fe(CN)_6]^{3-/4-}$ reaction (Figure S3, Supporting Information), and LNO is the most active for ORR. Suntivich et al. reported that a stronger covalency of the Ni–O bond should increase the driving force and thereby facilitate the O_2^-/OH^- exchange on the surface Ni ions, promoting the ORR activity.[15] Decreasing the A-site radius leads to tilting and rotation of the B-site octahedra, which decreases the Ni–O–Ni bond angle and thereby decreases the Ni–O hybridization (Figure 3b), resulting in the decreased ORR activity. And the ORR activity trend matches the conductivity of the $RNiO_3$ films (**Figure 5**), which is consistent with the early hypotheses of Meadowcroft and Matsumoto et al. that ORR catalysts must be conductive.[51,52] Moreover, the ORR activity was reported to be maximum for an e_g slightly less than one.[15] Considering that the e_g occupancy is 1 for stoichiometric LNO, any V_O formation due to strain and A-site isovalent substitution will lead to a value slightly higher than 1, consistent with the lower ORR activity measured here for $RNiO_3$ with oxygen vacancies induced by decreasing A-site radius.

On the other hand, the OER activity shows a complex trend with changing the A-site element in $RNiO_3$. Despite the conductive nature and covalent network, LNO is not the most active for OER; the incorporation of Nd (or mixtures of Nd and Sm) improves OER activity. The smaller rare-earth radius of Nd and Sm lead to the incorporation of more oxygen vacancies under the same synthesis and processing conditions, as seen by the change in OOP (Figure 2) and Ni
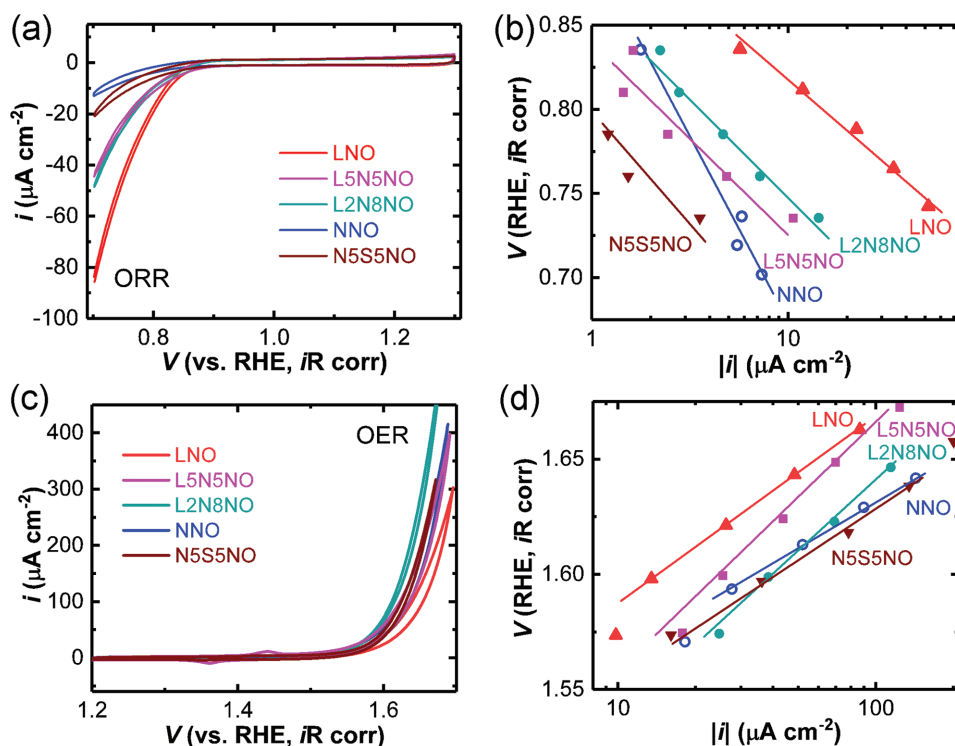

Figure 4. a,b) Electrochemical behavior of La- and Nd-containing nickelate films for ORR and c, d) OER in 0.1 M KOH saturated with O_2, normalized by the specific area with voltage corrected for the electrolyte resistance. a, c) CV at 10 mV s^{-1}. b, d) Tafel plot indicating the steady-state current obtained from CA as points with lines to guide the eye.

**ADVANCED
SCIENCE NEWS**

www.advancedsciencenews.com

**ADVANCED
FUNCTIONAL
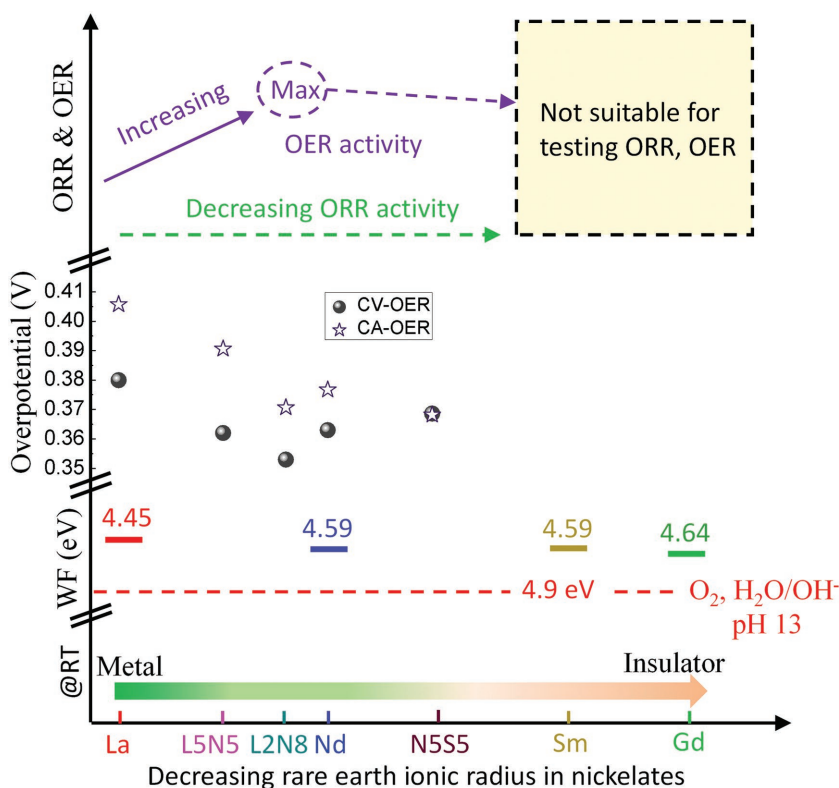MATERIALS**

www.afm-journal.de

Figure 5. Schematic illustration of the trends in the conductivity at RT, the WF values, the OER overpotential, and the ORR and OER activities with decreasing rare-earth ionic radius in nickelates. The red dashed line indicates the O_2, H_2O/OH^- redox level at pH 13. The OER overpotential is that required to obtain 40 µA cm^{-2} extracted from CV (spheres, swept polarization) or CA (stars, steady state). L2N8NO is the most active for OER, indicated by the smaller overpotential for OER. The OER uncertainty can be estimated as the difference in activity between these two measurement methods, with the *iR* correction being only ≈1 mV at 40 µA cm^{-2}.

L_2 edge (Figure 3). This trend is borne out of a decreasing energy of oxygen vacancy formation with tensile strain.[53] The corresponding reduction of Ni^{3+} to Ni^{2+} increases the average occupancy of the e_g antibonding orbital to more than one, reported favorable for an enhanced OER activity (e_g occupancy between 1 and 1.5) amongst ABO_3 perovskites.[16] Moreover, measurements of the WF of $RNiO_3$ films by UPS (Figure S5, Supporting Information) indicate that the Fermi level of $RNiO_3$ films shifts down with decreasing the A-site element radius, approaching the electrolyte redox level (4.90 eV) at pH 13, suggesting the positive signal for increasing the OER activity.[50] The extracted OER overpotential from CV and CA measurements also shows the decrease trend upon substituting La with Nd and is minimum for L2N8NO, indicating the most active OER for this sample. While the OER overpotential increases slightly for NNO, indicating a somewhat lower OER activity. Further reduction of the average A-site radius by substituting Nd with Sm gives comparable OER overpotential to NNO, consistent with the comparable OER activity shown in Figure 4d. Ongoing studies in our lab are investigating the impact of strain on $RNiO_3$ properties and activities. Further experimental investigations will address how to improve the catalysts activities of $RNiO_3$ films by hole-doping method.

3. Conclusion

In summary, we have investigated the structural, electronic properties, and ORR/OER activity of $RNiO_3$ thin films grown on $SrTiO_3$. Decreasing the A-site ionic radius bends the Ni–O–Ni bond angle, decreases the Ni–O hybridization and induces the electronic transition from metal to insulator at RT when changing the A-site element from La to Gd. We found that the ORR activity trend matches the conductivity of the $RNiO_3$ films, and both benefit from high Ni–O hybridization. Stronger Ni–O overlap should increase the driving force and thereby facilitate the O_2^-/OH^- exchange on the surface Ni ions, promoting the ORR activity. LNO is the most active for ORR, but not for OER. Substituting La with Nd (or mixtures of Nd and Sm) improves OER activity. Reducing the A-site radius of films coherently strained to STO lowers the energy of oxygen vacancy formation, resulting in a partial reduction of Ni^{3+} to Ni^{2+} with the incorporation of Nd into LNO. This increases the average occupancy of the e_g antibonding orbital to more than one, which promotes OER activity. We have presented a detailed study on the trends of ORR and OER activities for $RNiO_3$ films with different A-site elements and offer new understanding of the trade-offs in designing active bifunctional catalysts.

4. Experimental Section

Thin Film Growth: The RNO thin films were grown on the (001)-oriented STO and 0.7 wt% Nb-doped STO (Nb:STO) substrates by PLD. The laser fluence was ≈2 J cm^{-2} with a repetition rate of 5 Hz. The substrates were heated to 675 °C during deposition. The growth oxygen pressure (PO$_2$) was kept at 40 Pa and the growth rate was about 1 nm min^{-1}. After deposition, the samples were annealed in 10 kPa of oxygen for 10 min, and cooled down to RT. Heating/cooling rates of synthesis are 15 °C min^{-1}. One GNO film grown under PO$_2$ = 0.2 mTorr (GNO_0.2) was used as the reference sample for comparing the XAS data.

Electrical Measurements: For the electrical measurements, square Pt top electrodes of 400 µm × 400 µm and a thickness of 30 nm were deposited on the RNO films using a metal shadow mask. In-plane transport properties of RNO films were investigated using a 9 T PPMS (physical properties measurement system, Quantum Design) in the temperature range of 10–400 K. Linear four point geometry with Pt top electrodes was used.

Structural Characterization: AFM was used to examine the surface morphology of the RNO films. The crystallographic structures of these RNO films were investigated by high-resolution XRD from the X-ray Demonstration and Development beamline at the Singapore Synchrotron Light Source. The RSMs of RNO films were determined by using high-resolution XRD with a Philips X'Pert diffractometer equipped with a Cu anode.

XAS and UPS Measurements: XAS and UPS measurements were performed at the photoemission station at Beijing Synchrotron

Radiation Facility of Institute of High Energy Physics, Chinese Academy of Sciences. The ultrahigh vacuum chamber background pressure is about 2×10^{-10} Torr.

Electrochemical Experiments: GaIn eutectic (Sigma, >99.99%) was scratched into a corner of the RNO film, and a Cu wire held in contact with Ag paste (Liebsilber, Ted Pella). The wire contact, back and sides of the electrode were covered with inert epoxy (Locite 9460) such that only the RNO catalyst was exposed to the electrolyte. The 0.1 M KOH electrolyte was prepared from Nanopure water (18.2 MΩ cm) and KOH pellets (Sigma–Aldrich, 99.99%). The ≈15 mL volume was stirred and bubbled with ultra-high purity O_2 gas before and during data collection of the ORR and OER to fix the potential of oxygen redox.

Electrochemical measurements were conducted within a PFA cell with a CHI-660C or Biologic SP-200 potentiostat at 10 mV s^{-1}, and voltages corrected for the electrolyte/cell resistance from the high-frequency intercept of the real impedance (V–iR). The saturated calomel reference electrode (RE-2BP, ALS Co.) was calibrated to the reversible hydrogen electrode (RHE) scale in the same electrolyte and the Pt (ALS Co.) counter electrode. For measurements of in-plane voltage drop, 5×10^{-3} M each of $K_3Fe(CN)_6$ and $K_4Fe(CN)_6 \cdot 3H_2O$ (Sigma, >99%) were added to the 0.1 M KOH electrolyte, and the electrolyte saturated with ultra-high purity N_2 in a glass cell with a Ag/AgCl reference electrode (ALS Co.) calibrated to the RHE.

Supporting Information

Supporting Information is available from the Wiley Online Library or from the author.

Conflict of Interest

The authors declare no conflict of interest.

[1] N. S. Lewis, D. G. Nocera, *Proc. Natl. Acad. Sci. USA* **2006**, *103*, 15729.
[2] J. Greeley, N. M. Markovic, *Energy Environ. Sci.* **2012**, *5*, 9246.
[3] T. R. Cook, D. K. Dogutan, S. Y. Reece, Y. Surendranath, T. S. Teets, D. G. Nocera, *Chem. Rev.* **2010**, *110*, 6474.
[4] Z. F. Huang, J. Wang, Y. Peng, C. Y. Jung, A. Fisher, X. Wang, *Adv. Energy Mater.* **2017**, *7*, 1700544.
[5] V. R. Stamenkovic, D. Strmcnik, P. P. Lopes, N. M. Markovic, *Nat. Mater.* **2017**, *16*, 57.
[6] P. Strasser, *Acc. Chem. Res.* **2016**, *49*, 2658.
[7] Z.-L. Wang, D. Xu, J.-J. Xu, X.-B. Zhang, *Chem. Soc. Rev.* **2014**, *43*, 7746.
[8] J. K. Nørskov, J. Rossmeisl, A. Logadottir, L. Lindqvist, J. R. Kitchin, T. Bligaard, H. Jonsson, *J. Phys. Chem. B* **2004**, *108*, 17886.
[9] I. E. Stephens, A. S. Bondarenko, U. Grønbjerg, J. Rossmeisl, I. Chorkendorff, *Energy Environ. Sci.* **2012**, *5*, 6744.
[10] K. A. Stoerzinger, L. Qiao, M. D. Biegalski, Y. Shao-Horn, *J. Phys. Chem. Lett.* **2014**, *5*, 1636.
[11] C. C. McCrory, S. Jung, J. C. Peters, T. F. Jaramillo, *J. Am. Chem. Soc.* **2013**, *135*, 16977.
[12] C. C. McCrory, S. Jung, I. M. Ferrer, S. M. Chatman, J. C. Peters, T. F. Jaramillo, *J. Am. Chem. Soc.* **2015**, *137*, 4347.
[13] I. E. L. Stephens, J. Rossmeisl, I. Chorkendorff, *Science* **2016**, *354*, 1378.
[14] P. C. Vesborg, T. F. Jaramillo, *RSC Adv.* **2012**, *2*, 7933.
[15] J. Suntivich, H. A. Gasteiger, N. Yabuuchi, H. Nakanishi, J. B. Goodenough, Y. Shao-Horn, *Nat. Chem.* **2011**, *3*, 546.
[16] J. Suntivich, K. J. May, H. A. Gasteiger, J. B. Goodenough, Y. Shao-Horn, *Science* **2011**, *334*, 1383.
[17] C.-F. Chen, G. King, R. M. Dickerson, P. A. Papin, S. Gupta, W. R. Kellogg, G. Wu, *Nano Energy* **2015**, *13*, 423.
[18] J. R. Petrie, V. R. Cooper, J. W. Freeland, T. L. Meyer, Z. Zhang, D. A. Lutterman, H. N. Lee, *J. Am. Chem. Soc.* **2016**, *138*, 2488.
[19] W. T. Hong, M. Risch, K. A. Stoerzinger, A. Grimaud, J. Suntivich, Y. Shao-Horn, *Energy Environ. Sci.* **2015**, *8*, 1404.
[20] M. Risch, *Catalysts* **2017**, *7*, 154.
[21] J. Sunarso, A. A. Torriero, W. Zhou, P. C. Howlett, M. Forsyth, *J. Phys. Chem. C* **2012**, *116*, 5827.
[22] V. Celorrio, E. Dann, L. Calvillo, D. J. Morgan, S. R. Hall, D. J. Fermin, *ChemElectroChem* **2016**, *3*, 283.
[23] T. Hyodo, M. Hayashi, S. Mitsutake, N. Miura, N. Yamazoe, *J. Appl. Electrochem.* **1997**, *27*, 745.
[24] V. Celorrio, L. Calvillo, E. Dann, G. Granozzi, A. Aguadero, D. Kramer, A. E. Russell, D. J. Fermín, *Catal. Sci. Technol.* **2016**, *6*, 7231.
[25] K. A. Stoerzinger, W. Lü, C. Li, T. Venkatesan, Y. Shao-Horn, *J. Phys. Chem. Lett.* **2015**, *6*, 1435.
[26] J. R. Petrie, H. Jeen, S. C. Barron, T. L. Meyer, H. N. Lee, *J. Am. Chem. Soc.* **2016**, *138*, 7252.
[27] A. Grimaud, O. Diaz-Morales, B. Han, W. T. Hong, Y.-L. Lee, L. Giordano, K. A. Stoerzinger, M. T. Koper, Y. Shao-Horn, *Nat. Chem.* **2017**, *9*, 457.
[28] J. Kim, X. Yin, K.-C. Tsao, S. Fang, H. Yang, *J. Am. Chem. Soc.* **2014**, *136*, 14646.
[29] E. Tsuji, T. Motohashi, H. Noda, D. Kowalski, Y. Aoki, H. Tanida, J. Niikura, Y. Koyama, M. Mori, H. Arai, *ChemSusChem* **2017**, *10*, 2841.
[30] G. Catalan, *Phase Transit.* **2008**, *81*, 729.
[31] J. Chaloupka, G. Khaliullin, *Phys. Rev. Lett.* **2008**, *100*, 016404.
[32] J. Shi, Y. Zhou, S. Ramanathan, *Nat. Commun.* **2014**, *5*, 4860.
[33] M. Först, A. D. Caviglia, R. Scherwitzl, R. Mankowsky, P. Zubko, V. Khanna, H. Bromberger, S. B. Wilkins, Y.-D. Chuang, W. S. Lee, W. F. Schlotter, J. J. Turner, G. L. Dakovski, M. P. Minitti, J. Robinson, S. R. Clark, D. Jaksch, J.-M. Triscone, J. P. Hill, S. S. Dhesi, A. Cavalleri, *Nat. Mater.* **2015**, *14*, 883.
[34] L. Wang, S. Ju, L. You, Y. Qi, Y. Guo, P. Ren, Y. Zhou, J. Wang, *Sci. Rep.* **2015**, *5*, 18707.
[35] T. H. Kim, D. Puggioni, Y. Yuan, L. Xie, H. Zhou, N. Campbell, P. J. Ryan, Y. Choi, J.-W. Kim, J. R. Patzner, S. Ryu, J. P. Podkaminer,

ADVANCED
SCIENCE NEWS

www.advancedsciencenews.com

ADVANCED
FUNCTIONAL
MATERIALS

www.afm-journal.de

J. Irwin, Y. Ma, C. J. Fennie, M. S. Rzchowski, X. Q. Pan, V. Gopalan, J. M. Rondinelli, C. B. Eom, *Nature* **2016**, *533*, 68.

[36] Y. Zhou, X. Guan, H. Zhou, K. Ramadoss, S. Adam, H. Liu, S. Lee, J. Shi, M. Tsuchiya, D. D. Fong, S. Ramanathan, *Nature (London)* **2016**, *534*.

[37] I. C. Man, H. Y. Su, F. Calle-Vallejo, H. A. Hansen, J. I. Martínez, N. G. Inoglu, J. Kitchin, T. F. Jaramillo, J. K. Nørskov, J. Rossmeisl, *ChemCatChem* **2011**, *3*, 1159.

[38] Y. Kumar, R. Choudhary, S. Sharma, M. Knobel, R. Kumar, *Appl. Phys. Lett.* **2012**, *101*, 132101.

[39] L. Wang, L. Chang, X. Yin, L. You, J. Zhao, H. Guo, K. Jin, K. Ibrahim, J. Wang, A. Rusydi, J. Wang, *Appl. Phys. Lett.* **2017**, *110*, 043504.

[40] L. Wang, S. Dash, L. Chang, L. You, Y. Feng, X. He, K. Jin, Y. Zhou, H. G. Ong, P. Ren, S. Wang, L. Chen, J. Wang, *ACS Appl. Mater. Interfaces* **2016**, *8*, 9769.

[41] K. Zhang, P. Sushko, R. Colby, Y. Du, M. E. Bowden, S. A. Chambers, *Nat. Commun.* **2014**, *5*, 4669.

[42] L. Wang, Q. Zhang, L. Chang, L. You, X. He, K. Jin, L. Gu, H. Guo, C. Ge, Y. Feng, J. Wang, *Adv. Electron. Mater.* **2017**, *3*, 1700321.

[43] M. Pena, J. Fierro, *Chem. Rev.* **2001**, *101*, 1981.

[44] A. M. Deml, V. Stevanović, C. L. Muhich, C. B. Musgrave, R. O'Hayre, *Energy Environ. Sci.* **2014**, *7*, 1996.

[45] N. Palina, L. Wang, S. Dash, X. Yu, M. B. Breese, J. Wang, A. Rusydi, *Nanoscale* **2017**, *9*, 6094.

[46] E. J. Guo, Y. Liu, C. Sohn, R. D. Desautels, A. Herklotz, Z. Liao, J. Nichols, J. W. Freeland, M. R. Fitzsimmons, H. N. Lee, *Adv. Mater.* **2018**, *30*, 1705904.

[47] S. Middey, P. Rivero, D. Meyers, M. Kareev, X. Liu, Y. Cao, J. Freeland, S. Barraza-Lopez, J. Chakhalian, *Sci. Rep.* **2014**, *4*, 6819.

[48] M. Grisolia, J. Varignon, G. Sanchez-Santolino, A. Arora, S. Valencia, M. Varela, R. Abrudan, E. Weschke, E. Schierle, J. Rault, J.-P. Rueff, A. Barthélémy, J. Santamaria, M. Bibes, *Nat. Phys.* **2016**, *12*, 484.

[49] K. A. Stoerzinger, W. S. Choi, H. Jeen, H. N. Lee, Y. Shao-Horn, *J. Phys. Chem. Lett.* **2015**, *6*, 487.

[50] W. T. Hong, K. A. Stoerzinger, Y.-L. Lee, L. Giordano, A. Grimaud, A. M. Johnson, J. Hwang, E. J. Crumlin, W. Yang, Y. Shao-Horn, *Energy Environ. Sci.* **2017**, *10*, 2190.

[51] D. Meadowcroft, *Nature* **1970**, *226*, 847.

[52] Y. Matsumoto, H. Yoneyama, H. Tamura, *J. Electroanal. Chem.* **1977**, *83*, 237.

[53] A. Herklotz, D. Lee, E.-J. Guo, T. L. Meyer, J. R. Petrie, H. N. Lee, *J. Phys. Condens. Matter* **2017**, *29*, 493001.

[54] A. S. Disa, D. Kumah, J. Ngai, E. D. Specht, D. Arena, F. J. Walker, C. H. Ahn, *APL Mater.* **2013**, *1*, 032110.

[55] A. Ambrosini, J.-F. Hamet, *Appl. Phys. Lett.* **2003**, *82*, 727.

[56] J. A. Alonso, M. J. Martinez-Lope, M. T. Casais, M. A. Aranda, M. T. Fernandez-Diaz, *J. Am. Chem. Soc.* **1999**, *121*, 4754.

[57] Š. Masys, V. Jonauskas, *Comput. Mater. Sci.* **2015**, *108*, 153.

1803712 (8 of 8)